# Impacts of future urban expansion on summer climate and heat-related human health in eastern China

Qian Cao[a], Deyong Yu[a,*], Matei Georgescu[b], Jianguo Wu[a,c,**], Wei Wang[d]

[a] Center for Human-Environment System Sustainability, State Key Laboratory of Earth Surface Processes and Resource Ecology, Faculty of Geographical Science, Beijing Normal University, Beijing 100875, China
[b] School of Geographical Sciences and Urban Planning, Urban Climate Research Center, Arizona State University, Tempe, AZ 85287, United States
[c] School of Life Sciences and School of Sustainability, Arizona State University, Tempe, AZ 85287, United States
[d] Mesoscale & Microscale Meteorology Laboratory, National Center for Atmospheric Research, Boulder, CO 80301, United States

## ARTICLE INFO

## ABSTRACT

China is the largest and most rapidly urbanizing nation in the world, and is projected to add an additional 200 million city dwellers by the end of 2030. While this rapid urbanization will lead to vast expansion of built-up areas, the possible climate effect and associated human health impact remain poorly understood. Using a coupled urban-atmospheric model, we first examine potential effects of three urban expansion scenarios to 2030 on summer climate in eastern China. Our simulations indicate extensive warming up to 5 °C, 3 °C, and 2 °C in regard to low- (> 0%), high- (> 75%), and 100% probability urban growth scenarios, respectively. The partitioning of available energy largely explains the changes in 2-m air temperatures, and increased sensible heat flux with higher roughness length of the underlying urban surface is responsible for the increase of nighttime planetary boundary layer height. In the extreme case (the low-probability expansion pathway), the agglomeration of impervious surfaces substantially reduces low-level atmospheric moisture, consequently resulting in large-scale precipitation reduction. However, the effect of near-surface warming far exceeds that of moisture reduction and imposes non-negligible thermal loads on urban residents. Our study, using a scenario-based approach that accounts for the full range of urban growth uncertainty by 2030, helps better evaluate possible regional climate effects and associated human health outcomes in the most rapidly urbanizing areas of China, and has practical implications for the development of sustainable urban regions that are resilient to changes in both mean and extreme conditions.

## 1. Introduction

Urban expansion, the most evident expression of land-use/land-cover change, is recognized as a major modifier of local to regional climate (Mills, 2007). The most widely observed manifestation of urbanization-induced climate change is the urban heat island (Portman, 1993; Brazel et al., 2007; Myint et al., 2013), while urbanization effects on precipitation remain a complex subject (Shepherd et al., 2010; Niyogi et al., 2011; Wang et al., 2015). Aside from anthropogenic heat emissions in built-up areas (Salamanca et al., 2014; González and Gutierrez, 2015; Gutiérrez et al., 2015; Sailor et al., 2015), understanding the role of urban land existence in micro- and meso-scale climate has received increasing attention in the urban climate community (Georgescu et al., 2009a, 2009b; Grossman-Clarke et al., 2010; Cao et al., 2016; Sun et al., 2016b). For the non-desert environment,

urban growth decreases vegetation cover owing to contiguous increases in impervious surface. Along with high heat-storage capacity of constructed materials and impediments to atmospheric motion of the underlying surface, the structure of planetary boundary layer, hydrological cycle, and surface energy budget are modified accordingly, with additional consequences for temperature, air circulation, and precipitation change (Grimmond, 2007). As the recent United Nations projections show an increase in the world's urban population of 1.35 billion by 2030 (United Nations, 2012), it is clear that the influence of urbanization on climate will continue to increase (Grimm et al., 2008).

Although urban population growth is a global phenomenon, the bulk of urbanization and associated land modification will be concentrated in a few regions (Georgescu et al., 2015). Among these regions, Asia is anticipated to experience the most rapid growth of urban population by 2030, with China leading the way in this part of the

planet (Georgescu et al., 2015). Since the 1960s, megapolitan expansion, alone and separate from anthropogenic heating and external climate forcing, has contributed to one third of observed warming, 0.5 °C, in China (Sun et al., 2016b). By 2030, China is projected to add at least 200 million new city dwellers (Wu et al., 2014). The increase in urbanization rate will be inevitably manifest in the physical expansion of built-up areas. This, in turn, can further exacerbate the warming stress exerted on humans. While urban growth is expected to continue nationwide, the expanded built-up areas during 1992–2012 in the east of China were 4 to 20 times larger than those in the west that is characterized by uninhabitable plateaus and desert environments (Gao et al., 2015). Thus, future urban expansion will continue to proceed in eastern portions, with climate effects that require understanding to better aid planning and development.

Impacts of historical urban expansion on regional climate in China have been well documented by observation- (Zhou et al., 2004; Ren et al., 2008; Li et al., 2011; Song et al., 2014; Sun et al., 2016b) and modeling-based methods (Zhang et al., 2010; Feng et al., 2012; Wang et al., 2013; Wang et al., 2014; Cao et al., 2016). However, limited research exists focused on examination of climate effects owing to future urban expansion, which restricts our ability to alleviate the negative influence of this type of terrestrial modification. Recent work, however, is becoming increasingly aware of this limitation (Wang et al., 2016; Yang et al., 2016). The modeling work conducted was aimed at capturing future urban expansion-induced thermal impacts on major metropolises in China, such as Beijing, by investigating interactions between the urban canopy and overlying atmosphere. As a step forward, Chen and Frauenfeld (2016) assessed impacts of future urban expansion for China as a whole, via utility of a high-probability urban growth scenario derived from global projections of urban expansion, and found warming up to 3 °C on regional scale. However, due to uncertainties in underlying drivers, including GDP (Gross Domestic Product) and population estimates, projections of urban expansion contain a considerable degree of unpredictability. It is, therefore, necessary to incorporate these uncertainties into comprehensive climate change assessments.

Global projections of urban expansion provide probabilistic estimates of 2030 urban existence by integrating uncertainties introduced by GDP and population estimates (Seto et al., 2012). The spatially explicit data provide not only the amount but also the specific location of built-up areas for three potential types of future urban expansion across China: 100%, high-, and low-probability urban growth. Here we incorporate the aforementioned trio of scenarios into a process-based and coupled urban-atmospheric model to evaluate possible regional climate change impacts over the most rapidly urbanizing areas of the nation. Our focus of impacts is on the summer season because hundreds of millions of inhabitants in China's eastern portions endure their highest heat-related stress during this time of year. We aim at investigating the influences of land surface modification on regional climate of the highlighted regions. Our specific research objectives are focused on: (1) quantifying the amount and spatial distribution of urban expanse in 2030 according to three different urbanization scenarios; (2) estimating the effects of future urban expansion on summer climate in eastern portions of China; (3) assessing how these urbanization-induced climate changes translate to human thermal comfort impacts.

## 2. Materials and methods

### 2.1. Model configuration and parameterization

Simulations were performed using the Weather Research and Forecasting (WRF) Model with the advanced dynamical solver version 3.6.1 (Skamarock et al., 2008). The model was configured with a single domain having grid spacing of 20 km in both horizontal directions (Fig. 1). The domain was centered on 31°N and 117°E with 120 grid cells along east-west direction and 200 grid cells along north-south
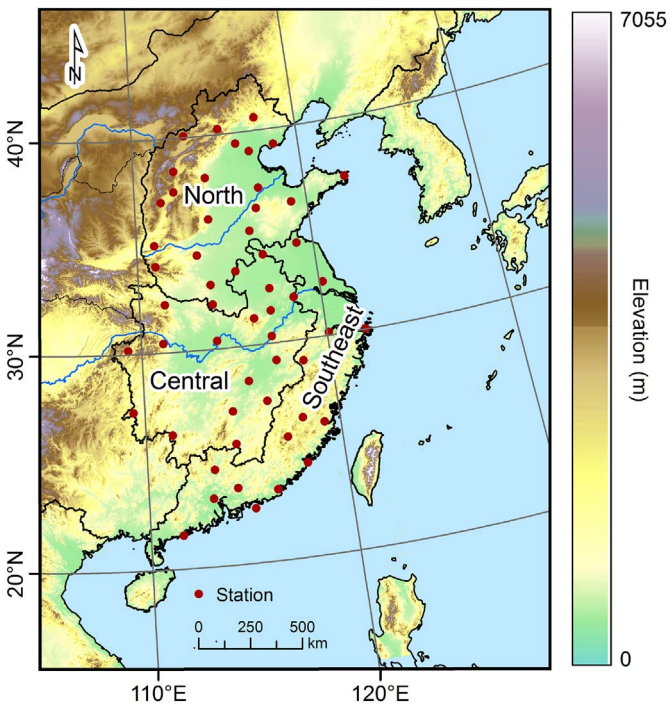


Fig. 1. Illustration of the model domain used in the WRF simulations with topography overlaid (m). The red points denote the international ground exchange meteorological stations in the study area (i.e., North, Central, and Southeast China). Note that the division of geographical regions in China is based on Liu et al. (2005). (For interpretation of the references to color in this figure legend, the reader is referred to the web version of this article.)

direction, embracing North, Central, Southeast China, and portions of the Pacific Ocean, with a total area of $2400 \times 4000 \text{ km}^2$. This domain configuration covered the three most rapidly urbanizing regions in China and was sufficiently expansive to capture the influence of the East Asian Monsoon on summer climate of the highlighted regions (Cao et al., 2016). The Lambert conformal conic projection was used for the model's horizontal coordinate and the model's vertical coordinate employed 30 terrain-following eta levels from the surface to 50 hPa.

The main physical parameterizations used for all simulations are presented in Table 1. In an attempt to represent urban land surface processes, the Noah land surface model (LSM; Chen and Dudhia, 2001; Ek et al., 2003) coupled with a single-layer urban canopy model (UCM;

**Table 1**
Main physical parameterizations used for all simulations.

| | |
|---|---|
| Model version: | Version 3.6.1 |
| Horizontal grid: | $\Delta X$ and $\Delta Y$ = 20 km |
| Number of points: | 120 (X direction), 200 (Y direction) |
| Vertical levels: | 30 levels |
| Time step: | 100 s |
| Radiation scheme: | RRTM[a] (longwave), RRTMG[b] (shortwave) |
| Land surface model: | Noah LSM |
| Urban surface model: | Single-layer urban canopy model |
| Cumulus scheme: | K-F[c] |
| Microphysics scheme: | WSM-3[d] |
| PBL scheme: | YSU[e] |
| Surface layer: | MM5 similarity[f] |
| Initial and lateral boundary conditions: | NCEP FNL/RTG_SST |

[a] RRTM, the Rapid Radiative Transfer Model.
[b] RRTMG, a new version of RRTM.
[c] K-F, the new Kain-Fritsch cumulus convective scheme.
[d] WSM-3, the WRF Single-Moment 3 class microphysics scheme.
[e] YSU, the Yonsei University planetary boundary layer (PBL) scheme.
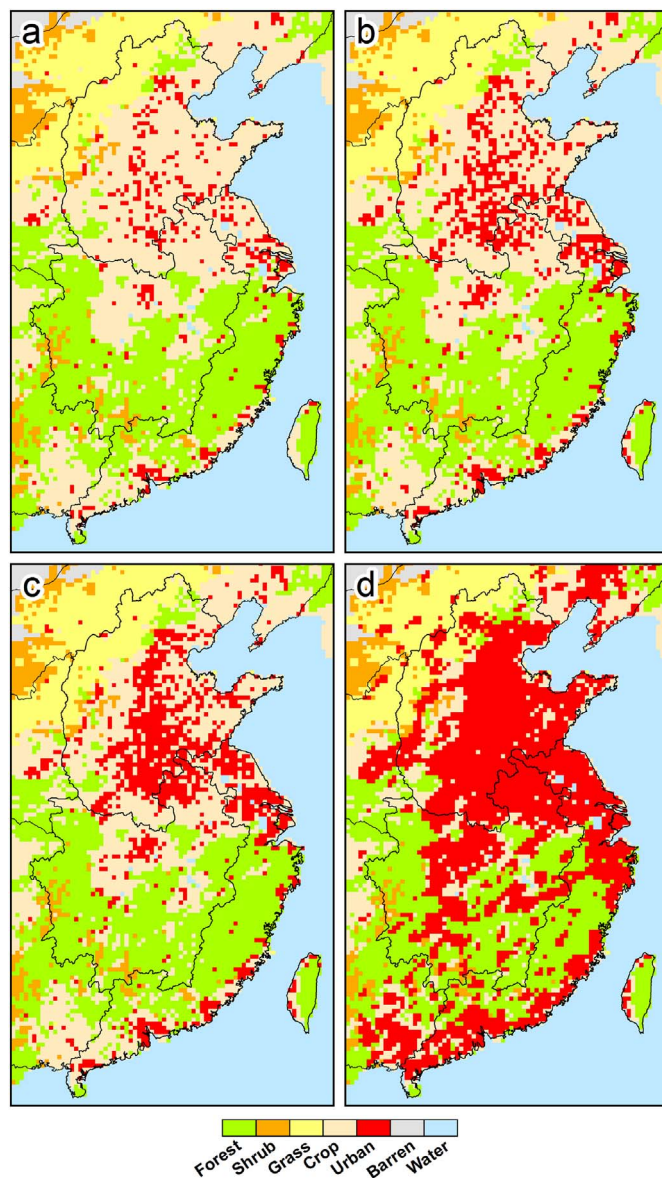[f] MM5, similarity, the revised MM5 Monin-Obukhov scheme.

**Fig. 2.** (a) Urban extent in 2010, (b) urban extent in 2030 with probability of grid cells that may become urban equal to 100%, (c) urban extent in 2030 with probability of grid cells that may become urban > 75%–100%, and (d) urban extent in 2030 with probability of grid cells that may become urban > 0%–100%.

Kusaka et al., 2001; Kusaka and Kimura, 2004) was selected to simulate the exchange of heat, momentum, and moisture between urban canopy and the atmosphere. The UCM has a simplified urban geometry with building height, road width, etc. specified for each urban subcategory. Here, we used the high-intensity residential class (i.e., 90% constructed materials versus 10% vegetation space) defined in the UCM to characterize built-up areas in China. We justify the rationale for this assumption based on the following two reasons. First, historical urban expansion in the nation during the past three decades was predominated by high-intensity urban growth (see Fig. 2 in Cao et al., 2016). Second, the pace of urbanization is anticipated to continue at a high rate in China to promote economic prosperity (Wu et al., 2014).

Initial and lateral boundary conditions for large-scale atmospheric fields were derived from the National Centers for Environmental Prediction (NCEP) Global Final Analysis (FNL) data archive, with a horizontal resolution of $1° × 1°$ and temporal interval of 6 h (http://rda.ucar.edu/). Because summer climate in eastern portions of China may be strongly influenced by the East Asian Monsoon, we actively

updated sea surface temperature (SST) during all simulations by incorporating data from NCEP's real-time and global SST analysis data archive (RTG_SST; ftp://polar.ncep.noaa.gov/) into the WRF model so as to improve the model's capability to simulate land-sea interactions. This approach has been demonstrated to generate better model performance compared with simulations utilizing prescribed SST (Cao et al., 2016). In order to have the retrieved SST updated every 6 h, the daily data were interpolated to a time interval of 6 h prior to the execution of WRF. Moreover, we assigned a diurnal cycle to the SST during all simulations.

### 2.2. Urban land cover data acquisition

Current urban land cover data corresponding to 2010 (hereafter Urb2010; Fig. 2a) were provided by the Data Center for Resources and Environmental Sciences, developed by the Chinese Academy of Sciences (http://www.resdc.cn/). A detailed description of the data and their incorporation into the WRF modeling system can be found in Cao et al. (2016).

Projected 2030 urban expanse was generated by Seto et al. (2012) based on population and GDP estimates, as well as existing population densities and built-up areas. The spatially explicit data provide probability estimates of whether a 5 km × 5 km grid cell will become urban by 2030, with 101 categories ranging between 0 and 100 (%), corresponding to the probability that a pixel may undergo urbanization. The projections exhibit three potential pathways of location specific future urban expansion in China: 100% urban growth (i.e., pixels with probability equal to 100% will be urbanized), high-probability urban growth (i.e., pixels with probability > 75% will be urbanized), and low-probability urban growth (i.e., pixels with probability > 0% will be urbanized; Fig. 2b–d), while the portion of pixels with probability between 25% and 75% only accounts for 4% of the total urbanized grid cells.

Here we selected pixels with urbanization probability equal to 100% to conservatively estimate urban existence in 2030 (hereafter Urb2030), > 75% to represent moderate urban growth (hereafter Urb2030_High), and > 0% to characterize extreme urban growth (hereafter Urb2030_Low). To enable use within WRF, the 5-km scenario data were aggregated to the domain resolution using the majority resampling technique (i.e., calculating the dominant land-cover type in each 20-km grid cell). It should be noted that only urban land cover was updated with the newly developed data. For other land-cover types, the default MODIS-based 20-category land-cover data, provided by the WRF modeling system, was used. Given the lack of information regarding projected non-urban landscape change, it was determined that this was a reasonable assumption.

As shown in Fig. 3, future urban expansion is expected to continue encroaching upon sizable arable lands in the eastern part of China. For the 100% and high-probability scenarios, the growth of urban areas is almost equivalent to the loss of cultivated lands. However, this does not seem to be the case for the low-probability scenario, where the number of farmlands reclaimed cannot compensate for the large-scale expansion of built environments. As a result, additional portions of forests distributed in Central and Southeast China necessitate removal in order to meet the demand for urban development.

### 2.3. Numerical simulation design

We designed four numerical experiments to investigate climate effects due to future urban expansion over the eastern portion of China, via incorporation of surface boundary conditions corresponding to Urb2010, Urb2030, Urb2030_High, and Urb2030_Low into the WRF modeling system, respectively (Table 2). The driving meteorology utilized for all simulations was identical so as to capture the urban expansion-induced signal. Concretely, each experiment was carried out for three consecutive years, initialized on January 1st, 2009 at 00:00
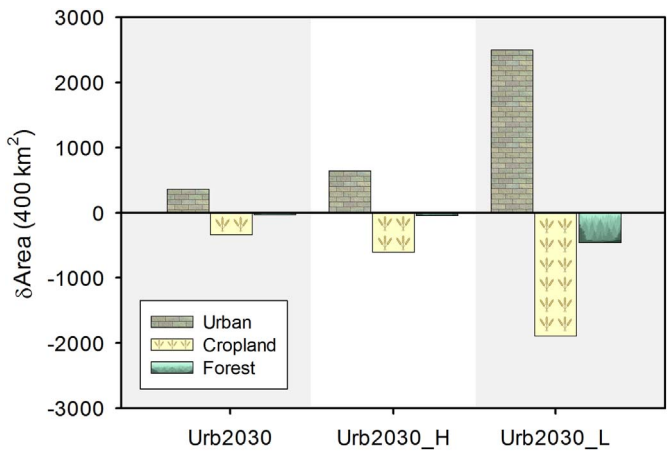
**Fig. 3.** Changes in urban, cropland, and forest areas from 2010 to 2030 in the region of interest (see Figs. 1–2) under the Urb2030, Urb2030_High, and Urb2030_Low scenarios.

**Table 2**
Description of all simulations performed.[a]

| Simulation | Spin-up period | Analysis time |
|---|---|---|
| Urb2010 | 1 Jan–28 Feb 2009 | 1 Mar 2009–1 Mar 2012 |
| Urb2030 | 1 Jan–28 Feb 2009 | 1 Mar 2009–1 Mar 2012 |
| Urb2030_High | 1 Jan–28 Feb 2009 | 1 Mar 2009–1 Mar 2012 |
| Urb2030_Low | 1 Jan–28 Feb 2009 | 1 Mar 2009–1 Mar 2012 |

[a] Urb2010: simulations using urban extent in 2010. Urb2030: simulations using projected urban extent in 2030 with probability of grid cells that may become urban equal to 100%. Urb2030_High: simulations using projected urban extent in 2030 with probability of grid cells that may become urban > 75%. Urb2030_Low: simulations using projected urban extent in 2030 with probability of grid cells that may become urban > 0%.

UTC and terminated on March 1st, 2012 at the same time. Output before February 28th, 2009 was considered as spin-up and therefore excluded from the following analysis. When illustrating summer climate effects owing to future urban expansion, all three summers derived from 2009, 2010, and 2011 simulations for a particular experiment were averaged and subsequently differentiated (e.g., Urb2030 – Urb2010). In addition, the standard deviation of appropriate metrics was calculated so as to provide a quantitative sense of simulated variability (Georgescu, 2015; Cao et al., 2016). In total, 12 simulations were performed in this work.

### 2.4. Model evaluation data

In order to evaluate the time-varying and spatially explicit model performance, both station-based and gridded observations were used in this work. Specifically, the station-based observations were obtained from the China international ground exchange stations through the China meteorological data service center (http://data.cma.cn/). The 194 exchange stations record daily meteorological information of mainland China from 1951 to present. Here, observed daily mean air temperature and precipitation accumulation, averaged across 2009, 2010, and 2011, were utilized to assess the time-varying model performance. Because of the relatively coarse grid spacing (i.e., 20 km) used for our simulations relative to location-based observations covering an area of 1 m$^2$, the observations were further averaged across all stations within each subregion (Fig. 1), and compared with the corresponding average of simulated grid cells, which were nearest to the station locations. This method is commonly used in the mesoscale modeling community given the resolution gap between observational stations and numerically modelled parameters (Salamanca et al., 2014; Georgescu, 2015; Cao et al., 2016).

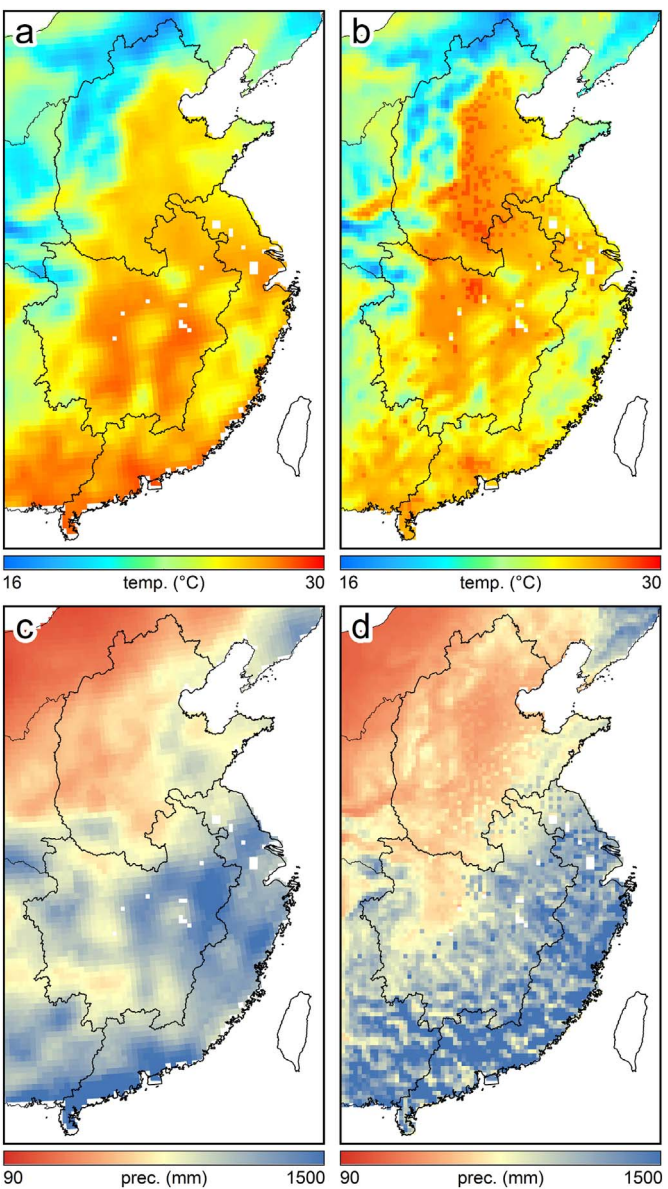The spatial evaluation of model performance was made against the



**Fig. 4.** Spatial pattern of (a) observed and (b) WRF-simulated mean 2-m air temperature (°C) and spatial pattern of (c) observed and (d) WRF-simulated mean precipitation (mm), averaged across all three summers (2009, 2010, and 2011), in North, Central, and Southeast China. The simulations are from Urb2010.

CN05.1 dataset, a gridded monthly air temperature and precipitation product available through the National Climate Center of China (http://ncc.cma.gov.cn/). The CN05.1 dataset was produced based on interpolation of 751 meteorological stations across mainland China for the purpose of climate model validation (Xu et al., 2009). It covers a period from 1961 to present, with a horizontal grid spacing of 0.25° in the x- and y-direction. To facilitate model examination, mean 2-m air temperature and precipitation, averaged from Urb2010 simulations across all three years (2009, 2010, and 2011), were compared with the corresponding gridded observations.

### 3. Results

#### 3.1. WRF model evaluation

A comparison of simulated summertime 2-m air temperature and precipitation from Urb2010 with the gridded observations demonstrated WRF's capability to capture reasonably well the spatial
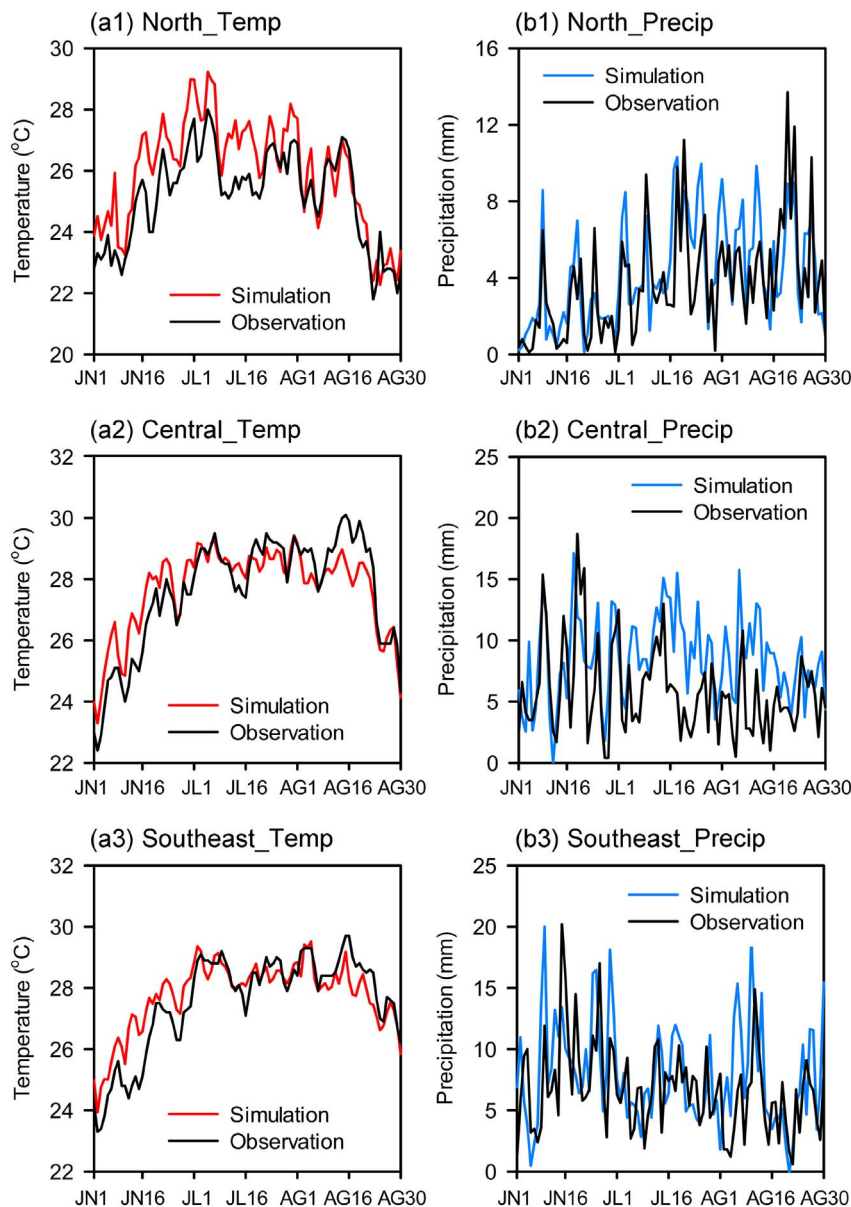
**Fig. 5.** Observed and WRF-simulated summertime daily mean time series of 2-m air temperature (°C; left column) and precipitation (mm; right column) in: (a1) and (b1) North China; (a2) and (b2) Central China; (a3) and (b3) Southeast China. The observations were averaged across all stations and three summers (2009, 2010, and 2011) in each subregion and compared with the corresponding average of simulated grid cells, which were nearest to the station locations.

variability of observations during the simulated time period (Fig. 4). Generally, the model successfully reproduced high temperature values in the plain areas of North, Central, and Southeast China, and low temperature values in the mountain areas of the northwestern part of the domain. Although a warm bias of ~2 °C was found in the North China Plain, the overall spatial correlation coefficient between the observations and simulations was 0.87. Similarly, the model represented the broad pattern of observed precipitation with reasonable fidelity. High precipitation values were appropriately simulated in Central and Southeast China and low precipitation values in North China and Inner Mongolia, with a spatial correlation coefficient equal to 0.73.

The simulated daily mean 2-m air temperature and precipitation accumulation also agreed well with the station-based observations for each of the subregions during the summer season (Fig. 5). When the observations exhibited a sharp increase in temperature or precipitation, the model followed the trend accordingly; conversely, when the observations indicated a steep decrease in temperature or precipitation, the model captured such changes appropriately. It is noteworthy that the performance of this version of the model parameterization has been evaluated for the three largest metropolitan agglomerations in China (i.e., Beijing-Tianjin-Hebei, Yangtze River Delta, and Pearl River Delta).

Simulation results demonstrated relatively better model performance compared with prior studies targeted on the same regions (Cao et al., 2016).

### 3.2. Impacts of future urban expansion on regional climate

We used ensemble differences in appropriate climate metrics to estimate the effects owing to projected 2030 urban expanse. The potential to exacerbate urbanization-induced warming differed substantially between scenarios (Fig. 6). Urban expansion, by eliminating arable lands completely (i.e., Urb2030_Low), resulted in local peak warming in excess of 5 °C. These impacts were especially evident in Central China, while extensive warming ranging between 3 and 4 °C was simulated for the majority of current and projected urban locales. Comparatively reduced warming, generally < 3 °C, was simulated under the high-probability scenario (i.e., Urb2030_High). The warming effects were further minimized spatially and quantitatively for the Urb2030 scenario (i.e., urban expansion restricted to those areas of highest likelihood), with increases in 2-m air temperatures generally between 1 and 2 °C. For all cases, near-surface warming in coastal locations was limited compared with inland areas, largely ascribed to the
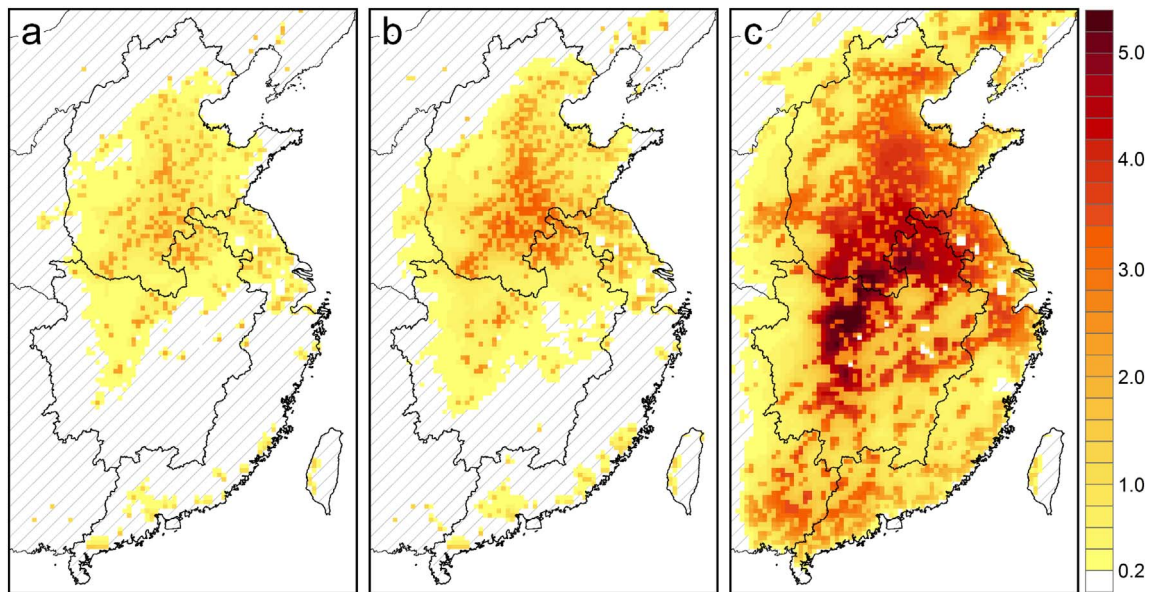
**Fig. 6.** Spatial pattern of WRF-simulated differences in summertime 2-m air temperature (°C) between 2010 and 2030 for all sensitivity experiments: (a) Urb2030 – Urb2010; (b) Urb2030_High – Urb2010; (c) Urb2030_Low – Urb2010.

influence of land-sea interactions. In addition, urban expansion led to the emergence of regional heat islands as impacts extended far beyond the built environment.

Differences in daytime maximum ($T_{max}$), nighttime minimum ($T_{min}$), and diurnal temperature range ($T_{rng} = T_{max} - T_{min}$), calculated only for urbanized grid cells in North, Central, and Southeast China, demonstrated the predominantly nighttime warming influence associated with projected urban expansion (Fig. 7). However, the spectrum of simulated impacts on $T_{rng}$ exhibited similar range (i.e., mean reduction of between 0.4 °C and 2.3 °C) regardless of the magnitude of urban growth. This was because the physical expansion of urban infrastructure in humid and semi-humid regions also contributed to non-negligible increases in $T_{min}$, with the amplification reaching 2–3 °C in the extreme case.

The pronounced increases in 2-m air temperatures identified previously did not occur at an equal rate during summer. On the contrary, time series of daily mean 2-m air temperature ($T_{avg}$) differences, once again calculated solely on urbanized locales, illustrated increased magnitude of warming through the season, with the rate of warming significantly (p value < 0.01) enhanced as built environments expanded (i.e., 0.1, 0.15, and 0.2 °C per 10 days for the three potential scenarios; Fig. 8). Furthermore, urban expansion markedly raised $T_{avg}$

from mid-July to the end of August (the hottest period of the year across the nation). With regard to the Urb2030 scenario, increased $T_{avg}$ was largely confined to 2 °C and the daily variability of $\Delta T_{avg}$ was minimal relative to the other two urban growth scenarios. In contrast, near-surface warming above 2 °C, on average, was simulated for Urb2030_Low, with a sharp increase in $T_{avg}$ of roughly 4 °C in late July (i.e., July 28–30) and mid-August (i.e., August 13–15). During these two periods, 2-m air temperatures in the eastern part of China rose to > 35 °C for the majority of urban grid cells (i.e., 72% for the July case and 63% for the August case). Based on the daily maximum temperature exceedance of 35 °C for > 3 consecutive days (China Meteorological Administration, http://www.cma.gov.cn), we characterize these two heatwave episodes (i.e., July 28–30; August 13–15) of high importance requiring further examination for heat-related health outcomes (see below).

We further examine alterations to surface energy budget components (i.e., surface-absorbed solar energy and the partitioning of available energy into sensible, latent, and ground heat fluxes) between the Urb2030_Low and Urb2030 pathways to improve understanding of the physical drivers of the simulated 2-m air temperature differences presented earlier. As shown in Fig. 9, the physical expansion of urban infrastructure reduced surface net radiation during the daytime. This
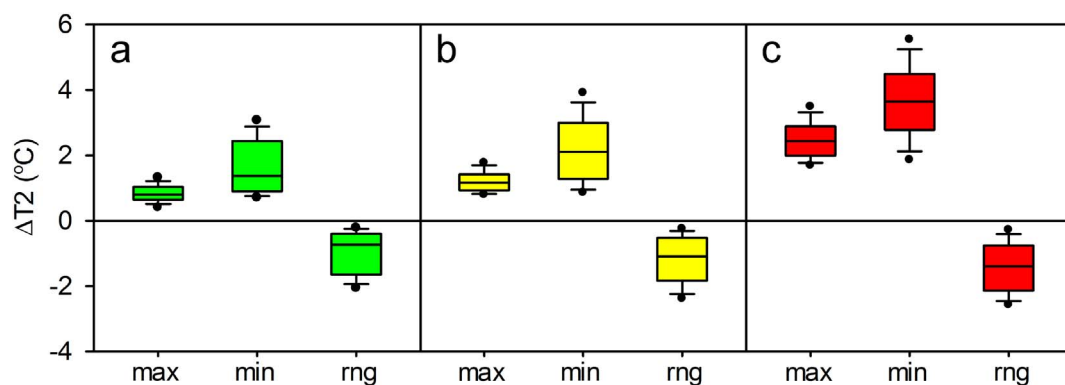


**Fig. 7.** Box-and-whisker plots of WRF-simulated differences in summertime 2-m air temperature (°C) daytime maximum ($T_{max}$; left of color trio), nighttime minimum ($T_{min}$; center of color trio), and diurnal range ($T_{rng} = T_{max} - T_{min}$; right of color trio) between 2010 and 2030 for all sensitivity experiments: (a) Urb2030 – Urb2010; (b) Urb2030_High – Urb2010; (c) Urb2030_Low – Urb2010. Calculations were performed only on urbanized grid cells in North, Central, and Southeast China. (For interpretation of the references to color in this figure legend, the reader is referred to the web version of this article.)
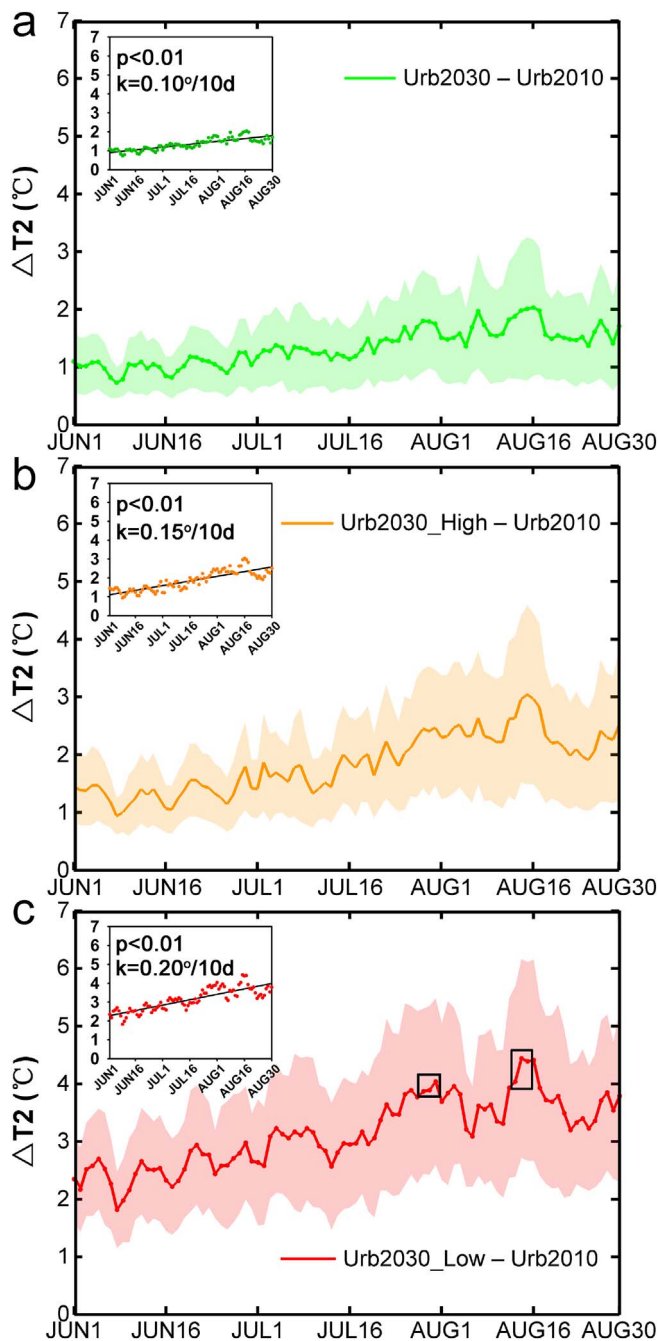
**Fig. 8.** WRF-simulated time series of daily mean 2-m air temperature differences (°C) between 2010 and 2030 for all sensitivity experiments: (a) Urb2030 – Urb2010; (b) Urb2030_High – Urb2010; (c) Urb2030_Low – Urb2010. The insets in each panel indicate trends of warming during summer. The shaded areas represent one standard deviation above and below the mean. The black rectangles marked in (c) indicate two heatwave events. Again, calculations were performed only on urbanized grid cells in North, Central, and Southeast China.



**Fig. 9.** WRF-simulated differences in summertime surface net radiation flux ($R_n$; W/m²), sensible heat flux (SH; W/m²), ground heat flux (GRD; W/m²), and latent heat flux (LH; W/m²) at 00:00, 06:00, 12:00, and 18:00 UTC (08:00, 14:00, 20:00, and 02:00 local standard time) between Urb2010 and Urb2030_Low. Note that negative GRD values indicate energy storage (i.e., energy loss from the atmosphere to the surface). Error bars represent one standard deviation above and below the mean. Calculations were performed only on urbanized grid cells in North, Central, and Southeast China.

The increased sensible heat flux, along with higher roughness length of the underlying surface, further deepened planetary boundary layer (PBL) height in built environments, with considerably larger nighttime than daytime changes (Fig. 10). In particular, increased magnitude of changes in PBL depth of up to 450 m, 620 m, and 730 m, respectively, was simulated for the three possible scenarios in the nighttime, compared with 230 m, 320 m, and 570 m in the daytime. The relatively small changes in daytime PBL depth are generally consistent with the comparatively reduced impacts on $T_{max}$ owing to the physically expanding urban infrastructure. As influenced by topography and land-sea interactions, changes in PBL depth also exhibited a notable gradient between inland and coastal areas. For example, elevated PBL height was < 300 m in general along the coastal zones in the case of Urb2030_Low, in contrast to 600–700 m inland.

Apart from higher 2-m air temperatures compared with the surroundings, urban expansion reduced low-level atmospheric moisture content (Fig. 11). For the Urb2030 and Urb2030_High scenarios, reduction in 2-m water vapor mixing ratio was generally restricted to 2 g/kg. However, for Urb2030_Low, a decrease of at least 2 g/kg in moisture was simulated for the majority of urban locales and as high as 4 g/kg over broader portions of urbanizing areas (it is noteworthy that under standard sea-level pressure, the water vapor content of a parcel of air at 25 °C with 50% relative humidity is 10 g/kg). The loss of moisture in the daytime was greater than that in the nighttime in the coastal belt due to land-sea interactions, whereas inland areas underwent a similar magnitude of moisture reduction during day and night. In the extreme case, the region displaying the largest decrease in 2-m water vapor mixing ratio was Central China. This region lies in the humid area of the nation (i.e., annual precipitation > 1000 mm) with high humidity for the duration of summer. In conjunction with the encroachment upon croplands, urban expansion imposed maximum impacts on low-level moisture there. Due to the distance from nearby water bodies, the loss of near-surface water vapor was not replaced as it was in coastal locations.

Finally, we used the ensemble differences in summer precipitation to illustrate how urbanization affected the hydrometeorological conditions of the highlighted regions (Fig. 12). Simulation results indicated that changes in the amount (Fig. 12a–b) as well as the fraction of precipitation (Fig. 12d–e) during summer were minor and negligible when the physical expansion of built environments was restricted to 100% and high (i.e., > 75%) likelihood probabilities. In other words, moderate growth of built-up areas, according to the simulation results

was because higher albedo of urban canopy, in our cases, reduced surface-absorbed downwelling shortwave radiation in the day. Sensible heat flux increased whereas latent heat flux decreased through day and night, with the latter exhibiting much greater daytime relative to nighttime effects. The reason was that the contiguous increase in impervious surface and thus decrease in vegetation cover in built-up areas substantially reduced evapotranspiration during the daytime. In addition, partitioning of available energy resulted in enhanced (energy) storage within the built environment during daylight hours and release during nighttime hours.
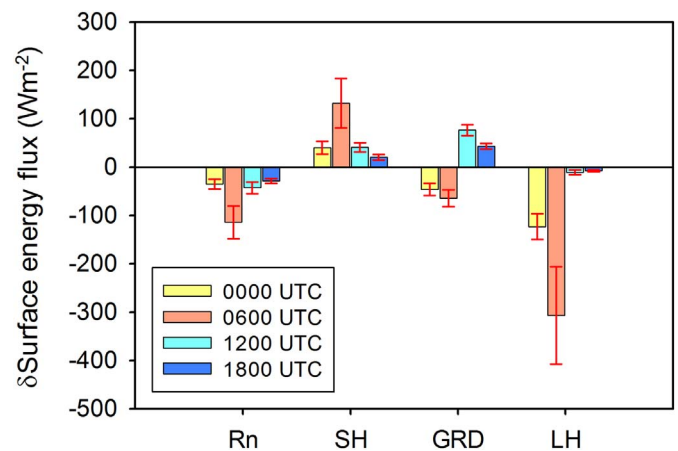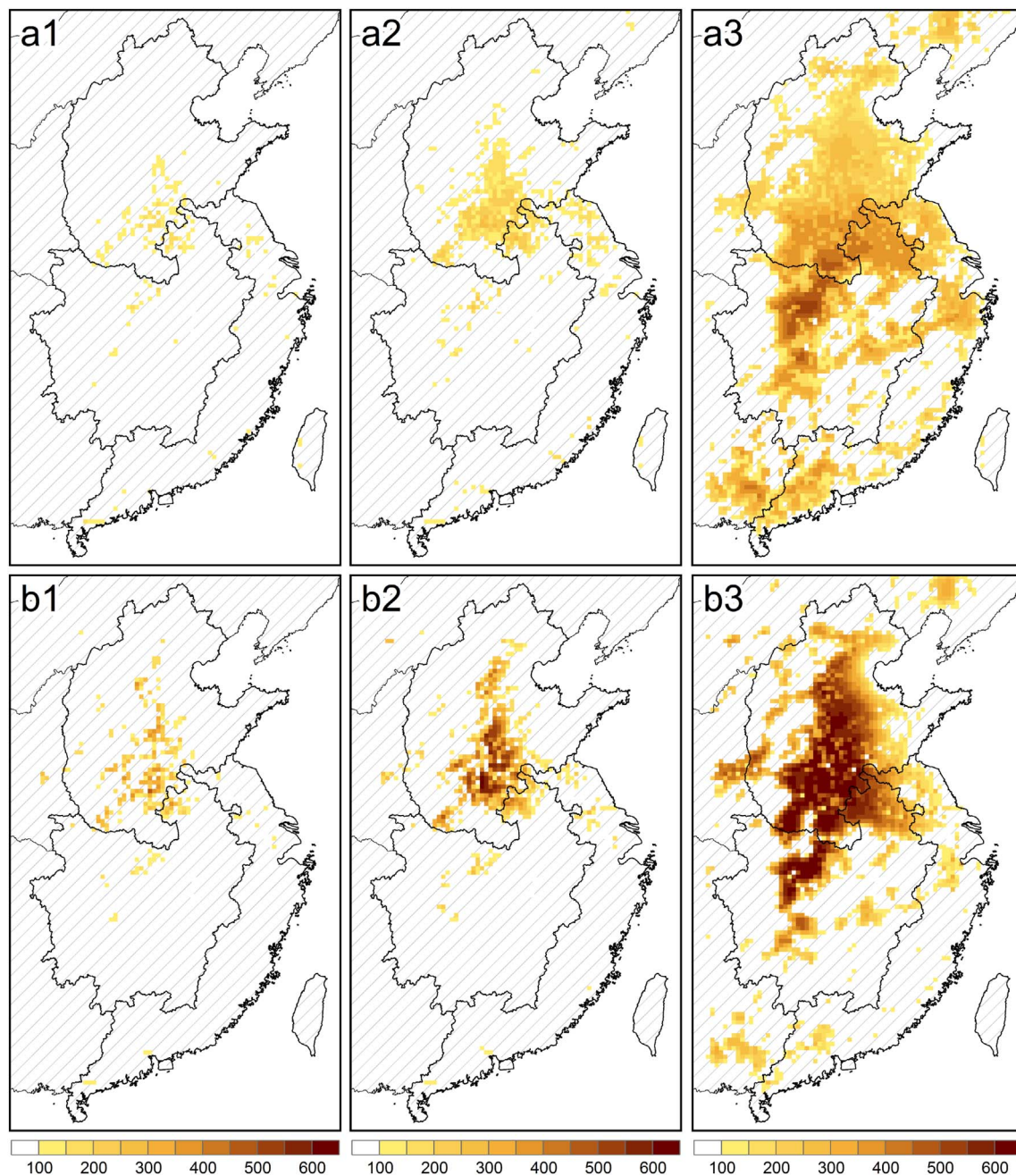
**Fig. 10.** WRF-simulated differences in summertime planetary boundary layer (PBL) height (m) between 2010 and 2030 for all sensitivity experiments in the daytime (the upper row) and nighttime (the lower row): (a1) and (b1) Urb2030 – Urb2010; (a2) and (b2) Urb2030_High – Urb2010; (a3) and (b3) Urb2030_Low – Urb2010.

presented here, would not alter the precipitation pattern in the rapidly expanding urbanized areas of China. However, an assessment of summer precipitation differences between Urb2010 and Urb2030_Low demonstrated the opposing effect. Widespread reduction in precipitation was simulated across nearly the entirety of North, Central, and Southeast China, with the reduction greater in the south than that in the north (Fig. 12c). On the contrary, the percentage decrease in precipitation exhibited the opposite trend, with the decrease larger in the north than that in the south (Fig. 12f).

### 3.3. Potential human health impacts of increased heat stress

The rising temperatures induced by urban expansion can further increase human health risk (i.e., heat-related morbidity and mortality). In view of this, we quantified the thermal loading of urban residents to assess how they would be affected by the considerable increase in temperatures. To date, numerous heat stress indices have been designed to evaluate the thermal comfort of human bodies (Willett and Sherwood, 2012), and all use temperature and humidity. Here, the wet-bulb globe temperature (WBGT) was selected because it is the ISO standard for quantifying thermal comfort and also the only heat stress index that has specific thresholds relating to levels of thermal risk (Willett and Sherwood, 2012). A WBGT value < 26 represents low thermal risk, between 26 and 28 moderate thermal risk, and > 28 high or extremely high (> 32) thermal risk. The simplified WBGT (hereafter W) is defined as $W = 0.567\,t + 0.393e + 3.94$, where $t$ is the air temperature in °C and $e$ the water vapor pressure in hPa.

As shown in Fig. 13, time series of summertime daily mean heat stress (calculated only on urbanized grid cells) for 2010 urban existence and the trio of 2030 urban growth scenarios exhibited increased
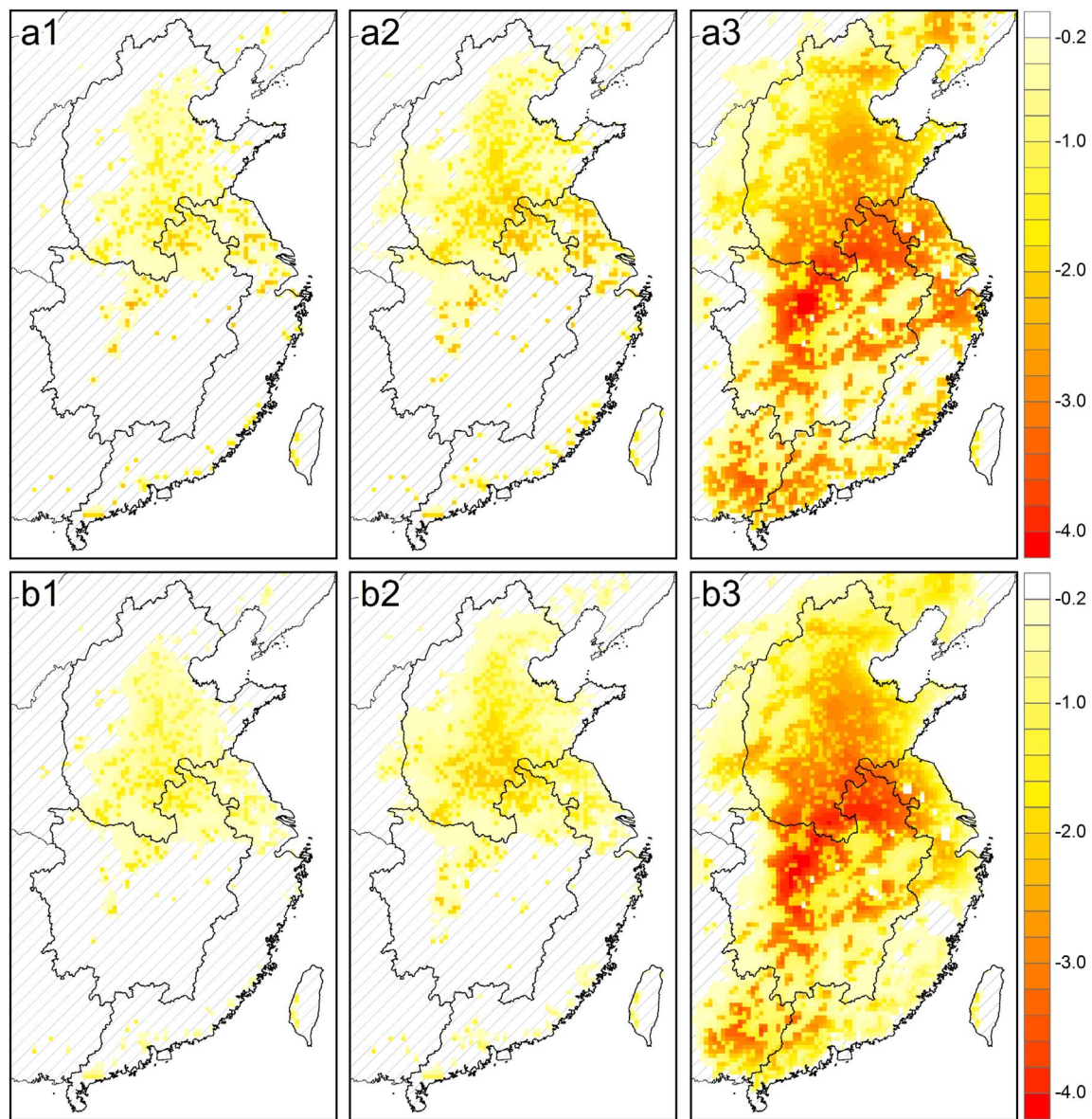
**Fig. 11.** WRF-simulated differences in summertime 2-m water vapor mixing ratio (g/kg) between 2010 and 2030 for all sensitivity experiments in the daytime (the upper row) and nighttime (the lower row): (a1) and (b1) Urb2030 – Urb2010; (a2) and (b2) Urb2030_High – Urb2010; (a3) and (b3) Urb2030_Low – Urb2010.

magnitude of thermal risk as built environments expanded. The most evident increases in heat stress were found during mid-July to mid-August, when 2-m air temperatures were highest. For Urb2030 and Urb2030_High, the heat stress was < 24, in general, whereas further urban expansion (i.e., Urb2030_Low) would raise the value above 25 in certain periods. This suggests that the thermal risk in specific locations may exceed beyond the threshold (i.e., W = 26) in such a case. Therefore, we further quantified the effects of the two heatwave events presented earlier (i.e., July 28–30; August 13–15) to help understand how urban residents would be impacted in the extreme case simulated here.

The geographical region whereby inhabitants suffer the greatest heat-related health risk was mainly confined to a triangle-shaped portion of east central China, as shown in Fig. 14. During July 28–30, W values in excess of 27 were evident across sizable locations, with the maximum reaching a value of 29 (Fig. 14a). Although heat stress in the northern part of Southeast China was generally < 26 (i.e., ~25.5), future background climate warming, in connection with urbanization-induced warming, may be expected to raise these values above the moderate threshold. A similar spatial pattern, but with decreased

magnitude of heat stress, was estimated for the period of August 13–15 (i.e., the other aforementioned heatwave event; Fig. 14b). During these days, W values did not exceed 28 for any locales. Moreover, the thermal risk potentially imposing on inhabitants in North China were weakened, whereas residents in Central China still confronted moderate heat-related health risk.

As urban environments bear the largest population density, it is valuable to assess how many people will be affected by such heatwaves (Fig. 14c). Here, population in 2030 was estimated from the shared socioeconomic pathway 2 (SSP2; http://www.cger.nies.go.jp/). This pathway is most likely to occur for China in the near future and we employ it here to conservatively estimate urban population through the end of 2030 (He et al., 2017), although as mentioned previously, quantifying the uncertainty of reduced likelihood urbanization has high value for the development of sustainable urban areas that are resilient to changes in both mean and extreme conditions. In this context, we estimated that approximately 400 million people (accounting for 1/3 of China's current population) would suffer thermal risk merely because of urban expansion (i.e., notwithstanding impacts due to greenhouse gas emissions and natural climate variability). Similar results have been
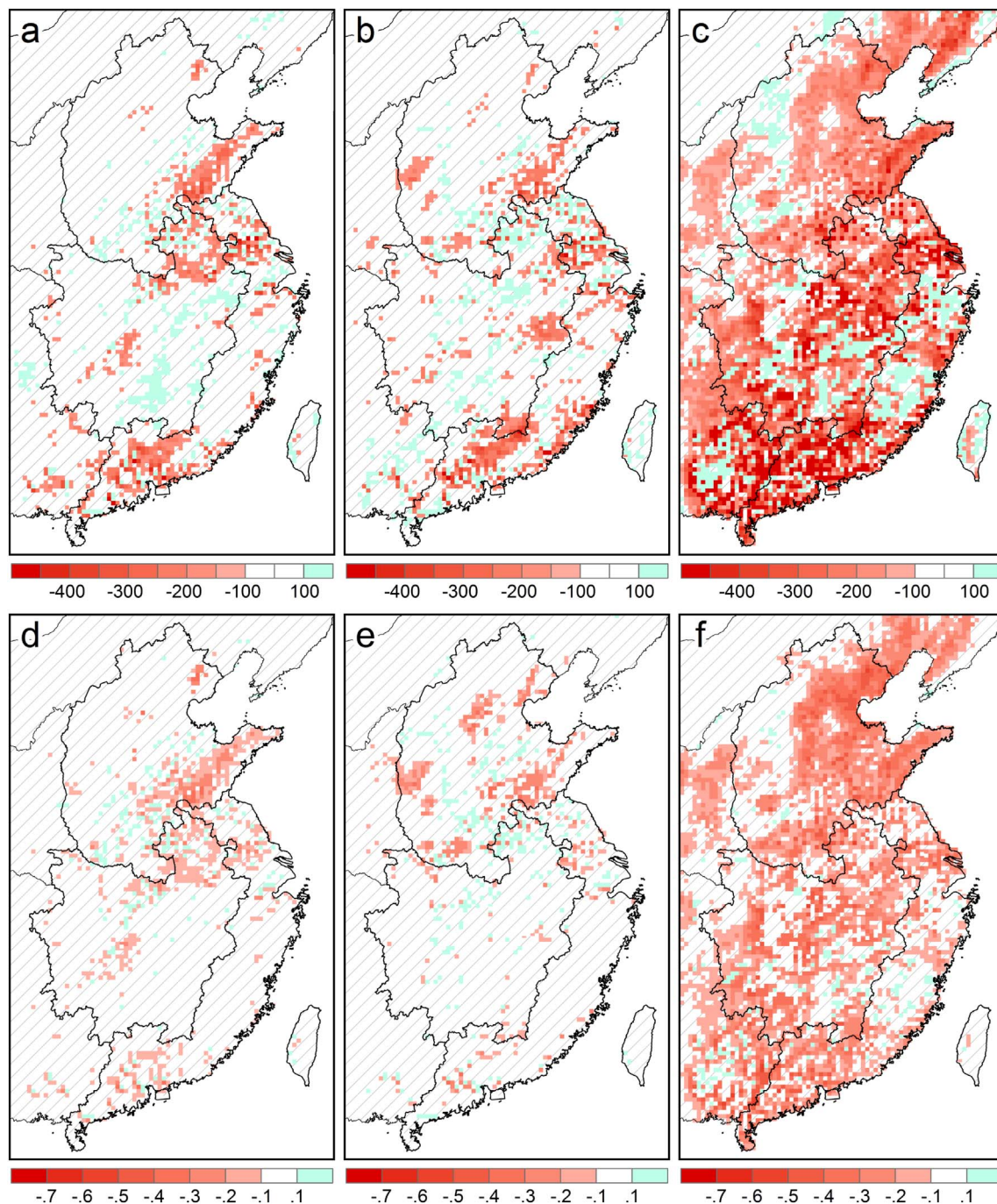
**Fig. 12.** WRF-simulated differences in summertime precipitation (mm; the upper row) and percentage changes in precipitation (%; the lower row) between 2010 and 2030 for all sensitivity experiments: (a) Urb2030 – Urb2010 and (d) (Urb2030 – Urb2010)/Urb2010; (b) Urb2030_High – Urb2010 and (e) (Urb2030_High – Urb2010)/Urb2010; (c) Urb2030_Low – Urb2010 and (f) (Urb2030_Low – Urb2010)/Urb2010.

concluded for other regions of the globe attempting to project heat stress changes in cities (e.g., Wouters et al., 2017).

## 4. Discussion

### 4.1. Impacts of future urban expansion on regional climate

Impacts on regional climate for future urban expansion through 2030 were examined for the most rapidly expanding urbanizing areas of China, i.e., North, Central, and Southeast China, through assessment of summertime variability of appropriate climate metrics (e.g., 2-m air temperature, precipitation, PBL height, and the surface energy budget

components). We estimated that near-surface warming resulting from low- (> 0%), high- (> 75%), and 100% probability urban growth was as high as 5 °C, 3 °C, and 2 °C, respectively, in eastern China, with central portions of the country undergoing the greatest increases in 2-m air temperatures. Our simulation results are in agreement with those of Chen and Frauenfeld (2016), a recent study reporting an increase in 2-m air temperatures approaching 3 °C by employing the high-probability urban growth scenario as lower boundary condition. It is known that a 2 °C global average temperature rise has become a jointly recognized mitigation target of the international community (UNFCCC, 2015). However, our study indicates that urban expansion alone, without the combined effects of increased emissions of long-lived greenhouse gases,
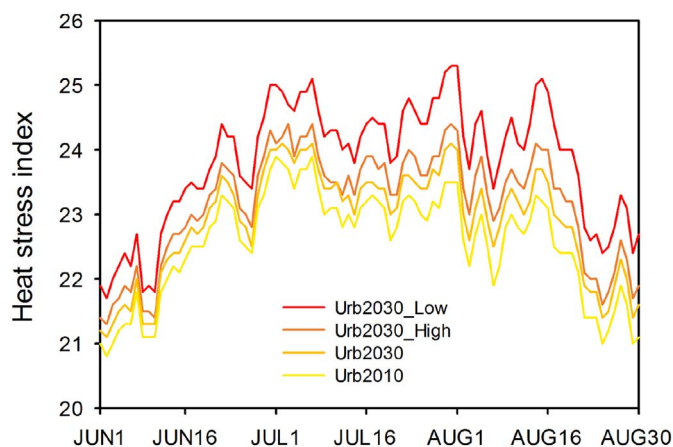
**Fig. 13.** WRF-simulated time series of summertime daily mean heat stress under the Urb2010, Urb2030, Urb2030_High, and Urb2030_Low scenarios. The heat stress was calculated using the simplified wet-bulb globe temperature (WBGT). Calculations were performed only on urbanized grid cells in North, Central, and Southeast China.

will bring about regional climate warming beyond that threshold. Therefore, the importance of the underlying urban surface on the overlying atmosphere should stimulate our attention, while achieving the goal of reducing greenhouse gas emissions.

Although urbanization effects on temperature are well-documented, its effects on precipitation and associated physical mechanisms remain elusive. Previous research indicated that urbanization may increase precipitation through the enhancement of convection (e.g., Chen et al., 2007; Shepherd et al., 2010; Miao et al., 2011; Niyogi et al., 2011), while recent studies are shedding new light on this particular subject (e.g., Wang et al., 2015; Benson-Lira et al., 2016; Zhang et al., 2017). For instance, Wang et al. (2015) found that the thermodynamical effects of urban expanse upon rainfall play a major role in the early stage of urbanization, while reduction in surface evapotranspiration and the resulting moisture deficit begin to take effect when built-up areas

continue to expand (e.g., urban agglomerations). The negative impacts of the latter may counteract the positive impacts of the former and thus lead to less rainfall in urban environments. This was especially evident in the extreme case (i.e., Urb2030_Low) presented here, where the large-scale replacement of vegetation cover by impervious surface substantially inhibited evapotranspiration and reduced low-level atmospheric moisture accordingly. For regions with insufficient water content like North China (with an annual precipitation generally < 800 mm compared with 1000–2000 mm in the Central and Southeast part), these urbanization impacts on regional precipitation and consequential water supply effects, demand our attention.

A deepened PBL is favorable to the dilution and diffusion of air pollutants (e.g., particular matter), although additional modifications to solar radiation, relative humidity, wind speed, etc. are likely to play further roles. However, our study was inconsistent with that of Georgescu (2015), whose urban expansion simulation (i.e., ICLUS_A2) revealed changes in PBL depth exhibiting larger daytime relative to nighttime effects. The reduction in daytime PBL depth, in Georgescu (2015), was in accord with the decrease in daytime 2-m air temperature. The discrepancy between the two modeling works may be attributed to the strong contribution of local background climate to the UHI phenomenon (Zhao et al., 2014). In arid regions, urban expansion can lead to decreased sensible heat flux and reduced maximum temperature during daylight hours, as a result of stronger energy storage by physical infrastructure (Lazzarini et al., 2015). However, for regions with cooler and wetter climate conditions, the heating capacity of urban canopy is restricted compared with arid areas. Therefore, portions of the absorbed daytime insolation will be partitioned into sensible heat flux that warms the air and results in an elevated PBL (Li et al., 2013).

Apart from background climate conditions, topography and land-sea interactions also contribute to shaping the magnitude and spatial pattern of changes in examined climate metrics. With regard to North and Central China, whose geographical locations abut against a range of high mountains (e.g., Taihang and Wu mountains), vertical heat/ moisture flux can dominate there with greater urban expansion-induced
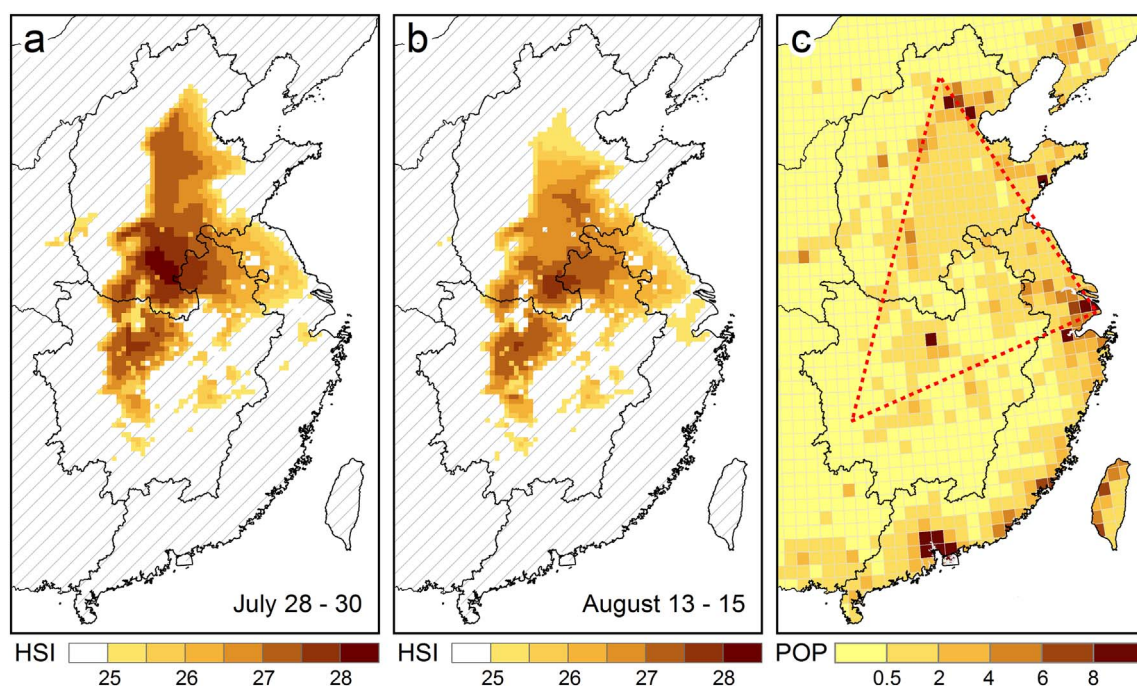


**Fig. 14.** Spatial pattern of heat stress in two heatwave events under Urb2030_Low scenario: (a) July 28–30 and (b) August 13–15. The heat stress was calculated using the simplified wet-bulb globe temperature (WBGT). A WBGT value < 26 represents low thermal risk, between 26 and 28 moderate thermal risk, and > 28 high thermal risk. Also shown is projected population (million) in 2030 under SSP2 scenario (c). The red dashed triangle in (c) outlines the number of people suffering heat-related health risk in heatwave days. (For interpretation of the references to color in this figure legend, the reader is referred to the web version of this article.)

climate effects compared with coastal zones. This is particularly true for the hinterland of North and Central China, where the influence of the summer monsoon is weakened. In contrast, Southeast China becomes strongly influenced by land-sea interactions for the duration of summer, facilitating the horizontal heat/moisture flux. Along with the transport of cool and moist air from the nearby sea, near-surface warming and drying effects are relatively modest there. As a consequence, it is easy to find distinct gradients in simulated impacts from inland to coastal areas. Therefore, it is necessary to incorporate real-time SSTs into long-term simulations, especially for monsoon-influenced regions like eastern China. Instead, their omission may fail to capture the spatial variability of climate effects (Cao et al., 2016).

### 4.2. Implications for future urban landscape planning

Our study highlights that the physical expansion of built-up areas would substantially warm regional environments and increase heat stress, a leading cause of weather-related morbidity and mortality. The situation gets worse when urban expansion markedly raised 2-m air temperatures during mid-July to the end of August, the hottest period of the year in the three urbanized regions. In fact, it is estimated that the rising frequency of heatwave events has already significantly increased mortality risk in China (Ma et al., 2015). This is especially unfavorable for the young and elderly, who are less able to regulate their bodies in extreme heat and must depend on others to provide required cool environments (Aubrecht and Özceylan, 2013). Even for the general population, such conditions can be exacerbated by sleep deprivation at night, when UHI effects are strongest. On local and regional scales, land surface modification can play a pivotal role in human health outcomes (Patz et al., 2005). As illustrated here, urban expansion alone can lead to extreme summer heat, without the added impact of greenhouse gases. Hence, adaptation strategies, including high albedo roofs (Susca et al., 2011; Georgescu et al., 2013, 2014, 2015; Sun et al., 2016a), permeable concrete or asphalt surface (Stempihar et al., 2012), or increased vegetation space (Kong et al., 2017; Sun and Chen, 2017), should be developed to alleviate the deleterious impacts of UHIs upon human health. This is particularly relevant for dwellers in Central China, where exposure to heat stress is anticipated to increase substantially.

Moreover, future urban expansion will continue to encroach upon sizable arable land in China. According to the Chinese Ministry of Agriculture (http://www.moa.gov.cn/), the grain product (i.e., corn, wheat, and rice) imports in China have increased by 490% so far and by 2020, food deficit in the nation will approach 100 million tons. China is becoming the world's largest food importer, which threatens the nation's food security. Although the likelihood of occurrence of the extreme urbanization case may be unlikely to take place in the future, it reminds us that the uncontrolled loss of farmland to fulfill rapid urbanization is an untenable pathway. One practical solution is to confine built-up areas by shifting urban expansion pattern from sprawl to infill as the growth rate of urban land in China is much higher than that of urban population (Gao et al., 2015). However, although current attitudes on sustainable cities endorse the notion of high-density patterns, there is no easy single way to achieve "resource-efficient and environment-friendly" urban landscapes when taking lifestyle choices plus housing energy and transportation fuel emissions into consideration (Heinonen et al., 2013a; Jalas et al., 2013b). Therefore, future work should also address how the intensity of urban infrastructure (e.g., building height, road density, green space, etc.) and the utility of energy (e.g., through increased use of air conditioning and the associated release of sensible and latent heat into outdoor environments) will affect urban climate and heat-related human health.

### 5. Conclusions

This study established a comprehensive assessment of how, and to

what extent, projected future urban expansion by 2030 would affect regional climate in North, Central, and Southeast China. Our model simulations revealed a magnitude of near-surface warming up to 2 °C, 3 °C, and 5 °C for 100%, high-, and low-probability urban growth scenarios, with Central China experiencing maximum increases in 2-m air temperatures and thus heat stress. In addition, summer precipitation was reduced across almost the entire eastern China under the low-probability urbanization pathway, while no appreciable changes in precipitation were detected for the 100% and high-probability pathways. Compared with prior study targeted on the effects of future urban expansion in China (i.e., Chen and Frauenfeld, 2016), our model simulations, with the explicit incorporation of multiple potential urban growth scenarios as surface boundary conditions, promote improved understanding of urban expansion impacts on regional climate, and underscore the importance of urban land surface on the lower atmosphere. These findings have practical implications for ameliorating deleterious aspects of urbanization on climate and human health (e.g., the UHI-related thermal loading) via urban landscape planning.

### Acknowledgements

### Competing interests

The authors declare no competing interests.

### References

Aubrecht, C., Özceylan, D., 2013. Identification of heat risk patterns in the US National Capital Region by integrating heat stress and related vulnerability. Environ. Int. 56, 65–77.

Benson-Lira, V., Georgescu, M., Kaplan, S., Vivoni, E.R., 2016. Loss of a lake system in a megacity: the impact of urban expansion on seasonal meteorology in Mexico City. J. Geophys. Res. Atmos. 121, 3079–3099.

Brazel, A., Gober, P., Lee, S.J., Grossman-Clarke, S., Zehnder, J., Hedquist, B., Comparri, E., 2007. Determinants of changes in the regional urban heat island in metropolitan Phoenix (Arizona, USA) between 1990 and 2004. Clim. Res. 33, 171–182.

Cao, Q., Yu, D., Georgescu, M., Wu, J., 2016. Impacts of urbanization on summer climate in China: an assessment with coupled land-atmospheric modeling. J. Geophys. Res. Atmos. 121, 10,505–10,521.

Chen, F., Dudhia, J., 2001. Coupling an advanced land surface-hydrology model with the Penn State-NCAR MM5 modeling system. Part I: model implementation and sensitivity. Mon. Weather Rev. 129, 569–585.

Chen, L., Frauenfeld, O.W., 2016. Impacts of urbanization on future climate in China. Clim. Dyn. 47, 345–357.

Chen, T., Wang, S., Yen, M., 2007. Enhancement of afternoon thunderstorm activity by urbanization in a valley: Taipei. J. Appl. Meteorol. Climatol. 46, 1324–1340.

Ek, M.B., Mitchell, K.E., Lin, Y., Rogers, E., Grunmann, P., Koren, V., Gayno, G., Tarpley, J.D., 2003. Implementation of Noah land surface model advances in the National Centers for Environmental Prediction operational mesoscale Eta model. J. Geophys. Res. Atmos. 108, D228851.

Feng, J., Wang, Y., Ma, Z., Liu, Y., 2012. Simulating the regional impacts of urbanization and anthropogenic heat release on climate across China. J. Clim. 25, 7187–7203.

Gao, B., Huang, Q., He, C., Ma, Q., 2015. Dynamics of urbanization levels in China from 1992 to 2012: perspective from DMSP/OLS nighttime light data. Remote Sens. 7, 1721–1735.

Georgescu, M., 2015. Challenges associated with adaptation to future urban expansion. J. Clim. 28, 2544–2563.

Georgescu, M., Miguez-Macho, G., Steyaert, L.T., Weaver, C.P., 2009a. Climatic effects of 30 years of landscape change over the Greater Phoenix, Arizona, region: 1. Surface energy budget changes. J. Geophys. Res. Atmos. 114, D05110.

Georgescu, M., Miguez-Macho, G., Steyaert, L.T., Weaver, C.P., 2009b. Climatic effects of 30 years of landscape change over the Greater Phoenix, Arizona, region: 2. Dynamical and thermodynamical response. J. Geophys. Res. Atmos. 114, D05111.

Georgescu, M., Moustaoui, M., Mahalov, A., Dudhia, J., 2013. Summer-time climate

impacts of projected megapolitan expansion in Arizona. Nat. Clim. Chang. 3, 37–41.

Georgescu, M., Morefield, P.E., Bierwagen, B.G., Weaver, C.P., 2014. Urban adaptation can roll back warming of emerging megapolitan regions. Proc. Natl. Acad. Sci. U. S. A. 111, 2909–2914.

Georgescu, M., Chow, W., Wang, Z., Brazel, A., Trapido-Lurie, B., Roth, M., Benson-Lira, V., 2015. Prioritizing urban sustainability solutions: coordinated approaches must incorporate scale-dependent built environment induced effects. Environ. Res. Lett. 10, 061001.

González, J.E., Gutierrez, E., 2015. On the environmental sensible/latent heat fluxes from A/C systems in urban dense environments: a new modeling approach and case study. In: ASME 2015 9th International Conference on Energy Sustainability collocated with the ASME 2015 Power Conference, the ASME 2015 13th International Conference on Fuel Cell Science, Engineering and Technology, and the ASME 2015 Nuclear Forum. American Society of Mechanical Engineers (pp. V002T17A005).

Grimm, N.B., Faeth, S.H., Golubiewski, N.E., Redman, C.L., Wu, J., Bai, X., Briggs, J.M., 2008. Global change and the ecology of cities. Science 319, 756–760.

Grimmond, S., 2007. Urbanization and global environmental change: local effects of urban warming. Geogr. J. 173, 83–88.

Grossman-Clarke, S., Zehnder, J.A., Loridan, T., Grimmond, C.S.B., 2010. Contribution of land use changes to near-surface air temperatures during recent summer extreme heat events in the Phoenix metropolitan area. J. Appl. Meteorol. Climatol. 49, 1649–1664.

Gutiérrez, E., González, J.E., Martilli, A., Bornstein, R., 2015. On the anthropogenic heat fluxes using an air conditioning evaporative cooling parameterization for mesoscale urban canopy models. J. Sol. Energy Eng. 137, 051005.

He, C., Li, J., Zhang, X., Liu, Z., Zhang, D., 2017. Will rapid urban expansion in the drylands of northern China continue: a scenario analysis based on the land use scenario dynamics-urban model and the shared socioeconomic pathways. J. Clean. Prod. 165, 57–69.

Heinonen, J., Jalas, M., Juntunen, J.K., Ala-Mantila, S., Junnila, S., 2013a. Situated lifestyles: I. How lifestyles change along with the level of urbanization and what the greenhouse gas implications are – a study of Finland. Environ. Res. Lett. 8, 025003.

Heinonen, J., Jalas, M., Juntunen, J.K., Ala-Mantila, S., Junnila, S., 2013b. Situated lifestyles: II. The impacts of urban density, housing type and motorization on the greenhouse gas emissions of the middle-income consumers in Finland. Environ. Res. Lett. 8, 035050.

Kong, L., Lau, K.K.L., Yuan, C., Chen, Y., Xu, Y., Ren, C., Ng, E., 2017. Regulation of outdoor thermal comfort by trees in Hong Kong. Sustain. Cities Soc. 31, 12–25.

Kusaka, H., Kimura, F., 2004. Coupling a single-layer urban canopy model with a simple atmospheric model: impact on urban heat island simulation for an idealized case. J. Meteorol. Soc. Jpn. Ser. II 82, 67–80.

Kusaka, H., Kondo, H., Kikegawa, Y., Kimura, F., 2001. A simple single-layer urban canopy model for atmospheric models: comparison with multi-layer and slab models. Bound.-Layer Meteorol. 101, 329–358.

Lazzarini, M., Molini, A., Marpu, P.R., Ouarda, T.B., Ghedira, H., 2015. Urban climate modifications in hot desert cities: the role of land cover, local climate, and seasonality. Geophys. Res. Lett. 42, 9980–9989.

Li, W., Chen, S., Chen, G., Sha, W., Luo, C., Feng, Y., Wen, Z., Wang, B., 2011. Urbanization signatures in strong versus weak precipitation over the Pearl River Delta metropolitan regions of China. Environ. Res. Lett. 6, 034020.

Li, D., Bou-Zeid, E., Barlage, M., Chen, F., Smith, J.A., 2013. Development and evaluation of a mosaic approach in the WRF-Noah framework. J. Geophys. Res. Atmos. 118, 11918–11935.

Liu, J., Liu, M., Tian, H., et al., 2005. Spatial and temporal patterns of China's cropland during 1990-2000: an analysis based on Landsat TM data. Remote Sens. Environ. 98, 442–456.

Ma, W., Zeng, W., Zhou, M., et al., 2015. The short-term effect of heat waves on mortality and its modifiers in China: an analysis from 66 communities. Environ. Int. 75, 103–109.

Miao, S., Chen, F., Li, Q., Fan, S., 2011. Impacts of urban processes and urbanization on summer precipitation: a case study of heavy rainfall in Beijing on 1 August 2006. J. Appl. Meteorol. Climatol. 50, 806–825.

Mills, G., 2007. Cities as agents of global change. Int. J. Climatol. 27, 1849–1857.

Myint, S.W., Wentz, E.A., Brazel, A.J., Quattrochi, D.A., 2013. The impact of distinct anthropogenic and vegetation features on urban warming. Landsc. Ecol. 28, 959–978.

Niyogi, D., Pyle, P., Lei, M., Arya, S.P., Kishtawal, C.M., Shepherd, M., Chen, F., Wolfe, B., 2011. Urban modification of thunderstorms: an observational storm climatology and model case study for the Indianapolis urban region. J. Appl. Meteorol. Climatol. 50, 1129–1144.

Patz, J.A., Campbell-Lendrum, D., Holloway, T., Foley, J.A., 2005. Impact of regional climate change on human health. Nature 438, 310–317.

Portman, D.A., 1993. Identifying and correcting urban bias in regional time series: surface temperature in China's northern plains. J. Clim. 6, 2298–2308.

Ren, G., Zhou, Y., Chu, Z., Zhou, J., Zhang, A., Guo, J., Liu, X., 2008. Urbanization effects on observed surface air temperature trends in North China. J. Clim. 21, 1333–1348.

Sailor, D.J., Georgescu, M., Milne, J.M., Hart, M.A., 2015. Development of a national anthropogenic heating database with an extrapolation for international cities. Atmos. Environ. 118, 7–18.

Salamanca, F., Georgescu, M., Mahalov, A., Moustaoui, M., Wang, M., 2014. Anthropogenic heating of the urban environment due to air conditioning. J. Geophys. Res. Atmos. 119, 5949–5965.

Seto, K.C., Güneralp, B., Hutyra, L.R., 2012. Global forecasts of urban expansion to 2030 and direct impacts on biodiversity and carbon pools. Proc. Natl. Acad. Sci. U. S. A. 109, 16083–16088.

Shepherd, J.M., Carter, M., Manyin, M., Messen, D., Burian, S., 2010. The impact of urbanization on current and future coastal precipitation: a case study for Houston. Environ. Plann. B 37, 284–304.

Skamarock, W.C., Klemp, J.B., Dudhia, J., Gill, D.O., Barker, D.M., Wang, W., Powers, J.G., 2008. A description of the advanced research WRF version 3 (no. NCAR/TN-475 + STR). In: NCAR Technical Note, http://dx.doi.org/10.5065/D68S4MVH.

Song, X., Zhang, J., AghaKouchak, A., Roy, S.S., Xuan, Y., Wang, G., He, R., Wang, X., Liu, C., 2014. Rapid urbanization and changes in spatiotemporal characteristics of precipitation in Beijing metropolitan area. J. Geophys. Res. Atmos. 119, 11,250–11,271.

Stempihar, J., Pourshams-Manzouri, T., Kaloush, K., Rodezno, M., 2012. Porous asphalt pavement temperature effects for urban heat island analysis. Transp. Res. Rec. 2293, 123–130.

Sun, R., Chen, L., 2017. Effects of green space dynamics on urban heat islands: mitigation and diversification. Ecosyst. Serv. 23, 38–46.

Sun, T., Grimmond, C.S.B., Ni, G.H., 2016a. How do green roofs mitigate urban thermal stress under heat waves? J. Geophys. Res. Atmos. 121, 5320–5335.

Sun, Y., Zhang, X., Ren, G., Zwiers, F.W., Hu, T., 2016b. Contribution of urbanization to warming in China. Nat. Clim. Chang. 6, 706–709.

Susca, T., Gaffin, S.R., Dell'Osso, G.R., 2011. Positive effects of vegetation: urban heat island and green roofs. Environ. Pollut. 159, 2119–2126.

UNFCCC, 2015. Decision 1/CP.21: adoption of the Paris Agreement. In: Paris Climate Change Conference, Paris.

United Nations, 2012. World Urbanization Prospects, the 2011 Revision. United Nations, New York Available at: http://esa.un.org/unpd/wup/index.htm, Accessed date: 6 March 2012.

Wang, M., Zhang, X., Yan, X., 2013. Modeling the climatic effects of urbanization in the Beijing-Tianjin-Hebei metropolitan area. Theor. Appl. Climatol. 113, 377–385.

Wang, X., Liao, J., Zhang, J., Shen, C., Chen, W., Xia, B., Wang, T., 2014. A numeric study of regional climate change induced by urban expansion in the Pearl River delta, China. J. Appl. Meteorol. Climatol. 53, 346–362.

Wang, J., Feng, J., Yan, Z., 2015. Potential sensitivity of warm season precipitation to urbanization extents: modeling study in Beijing-Tianjin-Hebei urban agglomeration in China. J. Geophys. Res. Atmos. 120, 9408–9425.

Wang, J., Huang, B., Fu, D., Atkinson, P.M., Zhang, X., 2016. Response of urban heat island to future urban expansion over the Beijing-Tianjin-Hebei metropolitan area. Appl. Geogr. 70, 26–36.

Willett, K.M., Sherwood, S., 2012. Exceedance of heat index thresholds for 15 regions under a warming climate using the wet-bulb globe temperature. Int. J. Climatol. 32, 161–177.

Wouters, H., De Ridder, K., Poelmans, L., et al., 2017. Heat stress increase under climate change twice as large in cities as in rural areas: a study for a densely populated midlatitude maritime region. Geophys. Res. Lett. 44, 8997–9007.

Wu, J., Xiang, W., Zhao, J., 2014. Urban ecology in China: historical developments and future directions. Landsc. Urban Plan. 125, 222–233.

Xu, Y., Gao, X., Shen, Y., Xu, C., Shi, Y., Giorgi, F., 2009. A daily temperature dataset over China and its application in validating a RCM simulation. Adv. Atmos. Sci. 26, 763–772.

Yang, L., Niyogi, D., Tewari, M., Aliaga, D., Chen, F., Tian, F., Ni, G., 2016. Contrasting impacts of urban forms on the future thermal environment: example of Beijing metropolitan area. Environ. Res. Lett. 11, 034018.

Zhang, N., Gao, Z., Wang, X., Chen, Y., 2010. Modeling the impact of urbanization on the local and regional climate in Yangtze River Delta, China. Theor. Appl. Climatol. 102, 331–342.

Zhang, Y., Miao, S., Dai, Y., Bornstein, R., 2017. Numerical simulation of urban land surface effects on summer convective rainfall under different UHI intensity in Beijing. J. Geophys. Res. Atmos. 122, 7851–7868.

Zhao, L., Lee, X., Smith, R.B., Oleson, K., 2014. Strong contributions of local background climate to urban heat islands. Nature 511, 216–219.

Zhou, L., Dickinson, R.E., Tian, Y., et al., 2004. Evidence for a significant urbanization effect on climate in China. Proc. Natl. Acad. Sci. U. S. A. 101, 9540–9544.